# Signatures of UV radiation around low-mass protostars in Serpens with IRAM 30 m

Agnieszka Mirocha[1,2], Agata Karska[2]★, Marcin Gronowski[3], Lars E. Kristensen[4], Miguel Figueira[5], Marcin Gładkowski[2,6], Łukasz Tychoniec[7], Michał Żółtowski[8]

[1] Astronomical Observatory of the Jagiellonian University, ul. Orla 171, 30-244 Kraków, Poland
[2] Institute of Astronomy, Faculty of Physics, Astronomy and Informatics, Nicolaus Copernicus University, ul. Grudziądzka 5, 87-100 Toruń, Poland
[3] Institute of Physical Chemistry Polish Academy of Sciences, ul. Kasprzaka 44/52, 01-224 Warszawa, Poland
[4] Centre for Star and Planet Formation, Niels Bohr Institute and Natural History Museum of Denmark, University of Copenhagen, Øster Voldgade 5-7, DK-1350 Copenhagen K, Denmark
[5] National Centre for Nuclear Research, ul. Pasteura 7, 02-093 Warszawa, Poland
[6] Nicolaus Copernicus Astronomical Center, ul. Rabiańska 8, 87-100 Toruń, Poland
[7] Leiden Observatory, Leiden University, P.O. Box 9513, NL-2300RA Leiden, The Netherlands
[8] University of Le Havre, Laboratoire Ondes et Milieux Complexes, UMR CNRS 6294,75 Rue Bellot, 76600 Le Havre, France

## ABSTRACT

*Context.* Ultraviolet radiation (UV) influences the physics and chemistry of star forming regions, but its properties and significance in low-mass protostars are still poorly-understood.

*Aims.* We aim to identify and characterise the UV radiation in the surroundings of low-mass protostars on $\sim 0.6 \times 0.6$ pc scales using the ratio of CN and HCN previously used for high-mass protostars. We focus on comparisons between protostar and outflow positions in the Serpens star-forming region and the validation of the proposed UV tracer for the corresponding physical conditions.

*Methods.* We present the $5' \times 5'$ maps of Serpens encompassing 10 protostars with EMIR on IRAM 30 m in CN 1-0, HCN 1-0, CS 3-2, and their isotopologues. Radiative-transfer code RADEX and the chemical model Nahoon are used to determine column densities of molecules, gas temperature and density, and the UV field strength, $G_0$.

*Results.* Spatial distribution of HCN and CS emission resembles the CO 6-5 from APEX tracing outflows. CN emission is spatially associated with the positions of protostars, yet also extends to their immediate surroundings. Detection of the line wings in CN profiles suggest that at least some emission is produced in the outflows, likely as a product of HCN photodissociation. The ratio of CN and HCN total column densities is in the range from 1 to 10 corresponding to $G_0$ of $10^{-3} - 10^{-2}$, for gas densities and temperatures typical for outflows of low-mass protostars.

*Conclusions.* UV radiation is identified towards both protostar and outflow positions, yet its strength is a factor of 10 lower than determined using OH and $H_2O$ ratios (Karska et al. 2018, ApJS). From the chemical viewpoint, the CN and HCN ratio is a more suitable tracer for UV fields characteristic for more massive protostars.

**Key words.** astrochemistry – stars: formation – ISM: molecules – ISM: individual objects: Serpens Main – Submillimeter: ISM

## 1. Introduction

Formation of low mass stars - the most numerous stellar population in galaxies (Kroupa 2002) - is associated with many physical phenomena. The inside-out collapse of dense envelopes is accompanied by the ejection of bipolar outflows and the formation of embedded disks (Frank et al. 2014; Harsono et al. 2015). UV radiation can be produced in accretion or bow shocks and irradiate the outflow cavities in the envelopes Spaans et al. 1995; van Kempen et al. 2009. The physical conditions and chemical composition in star forming regions strictly depend on the characteristics of the above processes.

The importance of UV radiation for star formation was initially considered only in the context of the formation of massive stars, where central stars are the main source of UV photons from early stages (Cesaroni 2005; Zinnecker & Yorke 2007).

Detail physico-chemical models of the envelopes and outflows with radiative transfer in 1 and 2D have been developed for high-mass protostars (Doty & Neufeld 1997; Stäuber et al. 2005; Bruderer et al. 2009). The far-UV radiation with photon energies < 13.6 eV dissociates and ionizes molecules and atoms with ionization potentials below 13.6 eV; more energetic photons are easily absorbed in the surrounding interstellar medium (Gerin et al. 2016). Among the most useful diagnostics of the UV field in dense envelopes are abundances of hydrides and the column density ratio of CN and HCN (Stäuber et al. 2007). The corresponding UV field strengths are enhanced by at least 1-2 orders of magnitude compared to the interstellar radiation field and impact gas at temperatures of few hundred K (Stäuber et al. 2007; Benz et al. 2016).

In low-mass protostars, the possible role of UV radiation was realised due to detection of narrow $^{12}$CO $J = 6 - 5$ lines spatially associated with outflow cavities in HH 46 van Kempen et al. (2009). Firm detection of [C I] 2-1 at the tip of the HH46 jet
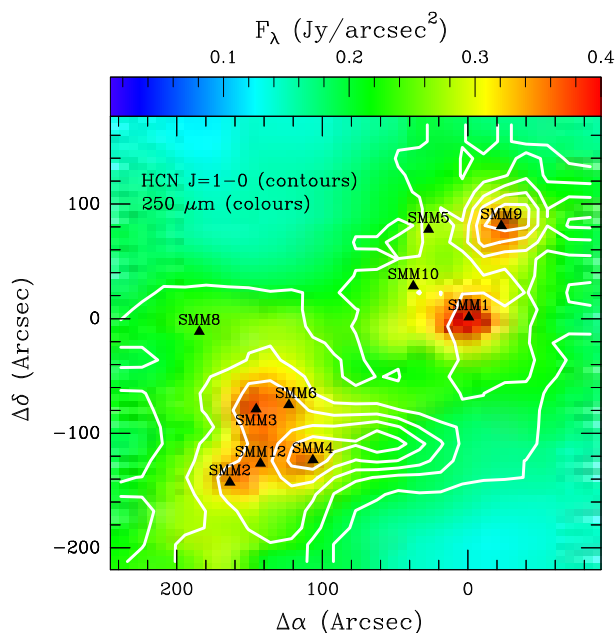
Fig. 1: EMIR map of HCN 1-0 (contours) on top of the continuum emission at 250 $\mu$m with *Herschel*/SPIRE. The HCN contours start at 0.4 K km s$^{-1}$ and are drawn in steps of 4 K km s$^{-1}$. Information about the protostars is shown in Table 1.

and the lack of CO was attributed to the presence of dissociative bow shock capable of producing extra UV photons (Neufeld & Dalgarno 1989). Their transport on $\sim$ 1000 AU scales is facilitated by the low densities and scattering in the outflow cavities (Spaans et al. 1995). Similar signatures of UV radiation were seen in a dedicated APEX CHAMP$^+$ survey of ~20 protostars (Yıldız et al. 2012, 2015).

Far-infrared observations with *Herschel* provided access to CO lines with $J_u$ up to 49, and resulted in the detection of new hydrides, e.g. OH$^+$ (Wyrowski et al. 2010) and H$_2$O$^+$ (Ossenkopf et al. 2010). As part of the 'Water in star-forming regions with Herschel' (WISH, van Dishoeck et al. 2011a) key program, a statistically significant sample of low-mass protostars was surveyed with the Heterodyne Instrument for the Far-Infrared (HIFI, de Graauw et al. 2010) and and the Photodetector Array Camera and Spectrometer (PACS, Poglitsch et al. 2010). Among the key findings are: (i) ubiquitous gas at temperature of *sim*300 K with molecular signatures resembling shocks (Herczeg et al. 2012; Goicoechea et al. 2012; Karska et al. 2013); (ii) a consistently low abundance of H$_2$O of $\sim$ 10$^{-6}$ (Kristensen et al. 2017); (ii) high abundances of the products of H$_2$O photodissociation and other hydrides, in particular OH (Wampfler et al. 2013; Benz et al. 2016); (iii) velocity-resolved components in H$_2$O profiles arising close to the protostar, at the positions of hydrides (Kristensen et al. 2013); (iv) ratios of H$_2$O/OH and CO/OH consistent with UV-irradiated shock models (Karska et al. 2018). All these pieces of evidence confirm the presence of UV photons in the immediate surroundings of low-mass stars.

In this paper, we analyze large-scale maps in HCN nad CN as alternative tracers of UV photodissociation in low-mass star forming region in Serpens to address the following questions: What is the morphology and spatial extent of the regions affected by UV radiation? Are there systematic differences in the ratios of CN and HCN between protostar and outflow positions? Does chemical models validate the utility of this ratio as a tracer of

UV-irradiated gas in regions forming low-mass stars? What is the typical strength of UV radiation in Serpens determined from CN and HCN, and how it compares to the results from *Herschel*?

The paper is organized as follows. §2 describes the studied region and its protostars, the observations and data reduction. §3 show the submillimeter maps and the line profiles at selected positions. §4 shows the determination of molecular column densities and their comparisons to the Nahoon chemical model. §5 discusses the results in the context of complementary studies and §6 presents the summary and conclusions.

## 2. Source sample and observations

### 2.1. Serpens as a low-mass star-formation site

The Serpens star forming region is a well-studied, low-mass site of star formation at the distance of 436±9 pc (Ortiz-León et al. 2017). The identification and classification of young stellar objects in the region was done as part of the *Spitzer* 'From Molecular Cores to Planet-forming Disks' (c2d) survey (Harvey et al. 2007; Enoch et al. 2009; Evans et al. 2009; Dunham et al. 2015). The outflow activity in the cloud core was characterized using CO 2-1 **[TBC!]** (Casali et al. 1993; Hurt & Barsony 1996; Testi & Sargent 1998; Davis et al. 1999), and more recently CO 3-2 and CO 6-5 for a subsample of sources (**Dionatos et al. 2010**, Yıldız et al. 2015). Ser SMM1, SMM3 and SMM4 were observed with *Herschel* as part of the WISH and 'Dust, Ice, and Gas in Time' (DIGIT, Green et al. 2013, 2016; Yang et al. 2018) programs.

Figure 1 shows the continuum map at 250 $\mu$m corresponding to the region that we observed with IRAM 30 m. The map was obtained with the *Herschel* Spectral and Photometric Imaging REceiver (SPIRE; Griffin et al. 2010) as part of the 'Herschel Gould Belt survey project' (André et al. 2010).

For the purpose of our analysis, we re-calculated spectral energy distributions (SEDs) for all protostars in the region using the continuum measurements at **70, 160 , 250, 350 and 500** $\mu$m from PACS and SPIRE covering the peak of the SEDs and following the procedures outlined in (**André et al. 2010**). Appendix A shows the final spectral energy distributions and provides the table with flux densities at each wavelength. Table 1 shows bolometric luminosities and temperatures, and the classification of the sources as Class 0 and I based on the later (Evans et al. 2009).

### 2.2. Observations and data reduction

The observations with IRAM 30 m were performed between 14$^{th}$ and 17$^{th}$ July 2009 as part of the project **'HCN/CN as UV-tracers in YSO envelope-outflow interfaces'** (PI: L. Kristensen). The Eight MIxer Receiver (EMIR) bands E090 and E150 covering 73-117 GHz and 125-184 GHz were used targeting HCN 1-0 and CN 1-0, respectively. The broad frequency ranges of EMIR facilitated additional detections of C$^{34}$S $3-2$, H$^{13}$CN $1-0$ and H$^{13}$CN $2-1$. The backend was the Versatile SPectrometer Array (VESPA) autocorrelator and the 1 MHz filterbank reaching the spectral resolution of 39 kHz (E150 band) and 78 kHz (E090 band). Table 2 shows the full list of transitions observed with EMIR with respective beam sizes and the main beam efficiencies used to convert antenna temperaturs to the main beam temperatures.

The OTF mode was used to obtain two maps with the sizes of 300$''$ × 300$''$ and map centers at $(\alpha_{J2000}, \delta_{J2000})$=18$^h$29$^m$49.6$^s$, +01°15'20.5$''$, and 18$^h$29$^m$56.6$^s$, +01°14'00.3$''$. Figure 2 shows the size and extent of the maps after the merging procedure and

Table 1: Luminosities and bolometric temperatures of targeted protostars in Serpens

| Source | R.A. (J2000.0) | Decl. (J2000.0) | $T_{bol}$ (K) | $L_{bol}$ ($L_\odot$) | Class | Other names |
|---|---|---|---|---|---|---|
| SMM 1 | 18 29 50.0 | +01 15 20.3 | 35 | 78.7 | 0 | Ser-emb6, FIRS1, EC41, Bolo23 |
| SMM 2 | 18 30 00.5 | +01 12 57.8 | 31 | 4.1 | 0 | Ser-emb4, Bolo28 |
| SMM 3 | 18 29 59.6 | +01 13 59.2 | 35 | 6.9 | 0 | Ser-emb26, Bolo26 |
| SMM 4 | 18 29 57.0 | +01 13 11.3 | 77 | 4.4 | I | Ser-emb22, Bolo25 |
| SMM 5 | 18 29 51.4 | +01 16 38.3 | 151 | 3.7 | I | Ser-emb21, EC53, WMW24, Bolo22 |
| SMM 6 | 18 29 57.8 | +01 14 05.3 | 532 | 43.1 | I | Ser-emb30, EC90, WMW35, SVS20S, Bolo 28 |
| SMM 8 | 18 30 01.9 | +01 15 09.2 | 15 | 0.2 | 0 | Bolo30 |
| SMM 9 | 18 29 48.3 | +01 16 42.7 | 35 | 10.3 | 0 | Ser-emb8, ISO241, WMW23, Bolo22 |
| SMM 10 | 18 29 52.3 | +01 15 48.8 | 83 | 6.2 | I | Ser-emb12, WMW21, Bolo 23 |
| SMM 12 | 18 29 59.1 | +01 13 14.3 | 97 | 5.7 | I | Ser-emb19, Bolo28 |

Source coordinates are adopted from Suresh et al. 2016 except of Ser SMM8, which position is listed in Lee et al. 2014).

Table 2: Catalog of the observed molecular lines with IRAM and APEX

| Mol. | Trans. | $E_u/k_B$ (K) | Freq. (GHz) | Telescope | Beam size (″) | Efficiency $\eta_{MB}$ |
|---|---|---|---|---|---|---|
| HCN | 1-0 | 4.25 | 88.631847 | IRAM-EMIR | 28 | 0.81 |
| H$^{13}$CN | 1-0 | 4.14 | 86.340184 | IRAM-EMIR | 29 | 0.81 |
| | 2-1 | 12.43 | 172.677881 | IRAM-EMIR | 14 | 0.68 |
| CN | 1-0 | 5.45 | 113.490985 | IRAM-EMIR | 22 | 0.78 |
| C$^{34}$S | 3-2 | 13.9 | 144.617109 | IRAM-EMIR | 16 | 0.74 |
| CS | 3-2 | 14.1 | 146.969029 | IRAM-EMIR | 16 | 0.74 |
| $^{12}$CO | 6-5 | 116.2 | 691.473076 | APEX-CHAMP+ | 9 | 0.48 |

Molecular data adopted from the Leiden Atomic and Molecular Database (LAMDA, Schöier et al. 2005) and the JPL database (**Pickett et al. 1998**).

beam convolution. The merging and data reduction was carried out with the CLASS package within GILDAS[1]. For the sake of analysis, the EMIR spectra were baseline-corrected and resampled to a resolution of 0.5 km/s. The rms of extracted spectra varies from 0.024 K to 0.125 K.

**CHAMP+ (Kasemann et al. 2006, Güsten et al. 2008) on Atacama Pathfinder Experiment (APEX) was used for CO 6-5 observations at 691.5 GHz. This is a heterodyne receiver of two arrays allowing to observe simultaneously in the 650 GHz and 850 GHz bands. The Fast Fourier Transform Spectrometer (FFTS) was used as the backend [? information from (Yıldız et al. 2015)] with a resolution of 0.079 km s$^{-1}$ (Klein et al. 2006). Spectra were converted to the main-beam brightness temperature $T_{mb}$ using beam efficiency $\eta_{mb}$ = 0.56.**

**The observations were performed on June 16$^{th}$ 2009 with position-switching in on-the-fly mapping mode resulting in maps covering 340″ × 340″. The beam size of APEX is 9.1″ at 691.5 GHz. Typical value of rms is ≈ 0.018 K. Similar procedure of data reduction and analysis with CLASS software was implemented to APEX data as well.**

## 3. Results

In the following sections, we present IRAM 30 m maps and line profiles providing complementary information about the emission from protostars and their outflows, and large-scale cloud emission. Differences in spatial extent reflect the range of gas

and dust distribution and associated physical conditions and processes. We calculate ratios of various transitions to pin-point species tracing similar physical components, the gas temperature, and line opacities.

### 3.1. Spatial extent of line emission

Figure 2 shows the line emission associated with protostars and their outflows in Serpens obtained in HCN, CN, CS lines with EMIR on IRAM 30 m and CO with CHAMP$^+$ on APEX. The emission in HCN and CN is the sum of all hyperfine components detected in the spectra (see Figure 3.2). Maps in additional transitions are presented in Appendix B.

HCN 1-0 emission, similar to other species, is associated with clusters of protostars in the SE and NW parts of the map where dust emission at 250 $\mu$m is also detected (Figure 1). The emission peaks are the strongest at the positions of Ser SMM4 and SMM9 protostars and their outflows, and significantly weaker at Ser SMM1 and SMM3. Qualitatively, the pattern of emission in HCN is similar to the CO 6-5 - the well-established outflow tracer (Figure 2; bottom right panel). This results is in agreement with previous surveys of HCN in low-mass protostars (Bachiller et al. 2001; Walker-Smith et al. 2014). Any differences between HCN and CO likely stem from the higher critical density of the HCN 1-0 (~ $10^6$ cm$^{-2}$), its lower upper energy level (see Table 2), and its significantly easier photodissociation due to UV photons than CO (see §5).

CS 3-2 emission shows a very similar spatial distribution to HCN 1-0 and CO 6-5, with most prominent structures associated with Ser SMM4. Some differences are seen mostly in the
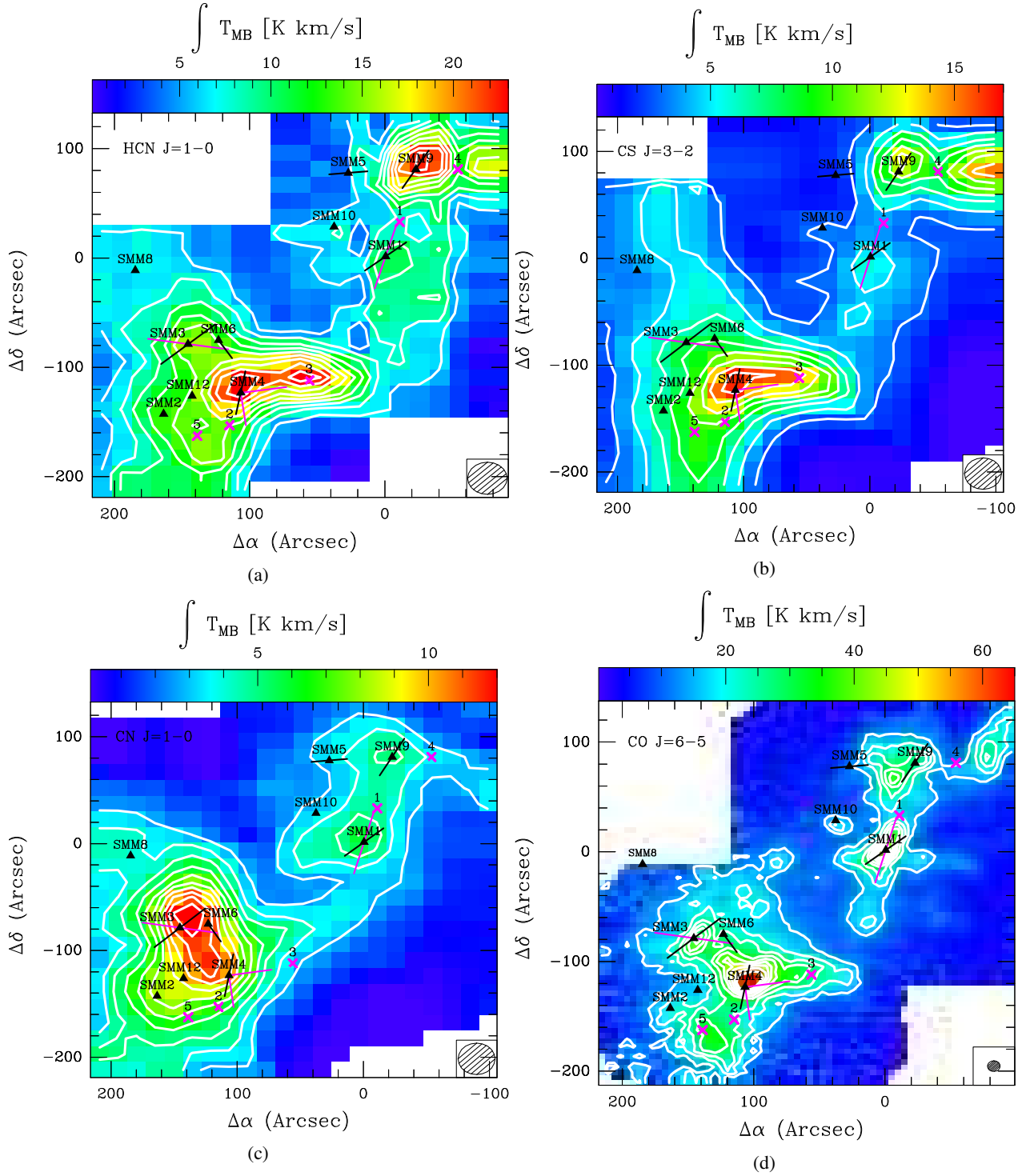
Fig. 2: Integrated intensity maps of the HCN 1-0 (upper left panel), CS 3-2 (upper right panel), CN 1-0 (bottom left panel) and CO 6-5 (bottom right panel) in Serpens star-forming region with IRAM 30 m. Black triangles show the positions of protostars (see Table 1) and magenta crosses show the outflow positions selected for analysis (see Table 3). Solid lines show outflow directions from CO 6-5 (black; Yıldız et al. 2015) and CO 3-2 (magenta; Dionatos et al. 2010). The center of the maps (0,0) corresponds to (RA, DEC)= $18^h29^m46.6^s$, $01°18'20.5''$. Contour levels start at 30 $\sigma$ for HCN and CN and increase every 10 $\sigma$. For CS and CO, the first contours are at 10 $\sigma$ and 70 $\sigma$ levels, and the steps are 5 $\sigma$ and 30 $\sigma$, respectively.

surrounding of Ser SMM9, where CS emission is substantially weaker at the Ser SMM9 position than in Ser SMM4, in contrast to HCN which shows similar line strengths towards both protostars. Additionally, CS shows a relatively strong emission to the W of Ser SMM9, which coincides with the outflow from S68N

- with the protostar itself located outside of the map (Kristensen et al. 2010). The differences may result from CS tracing warmer, yet lower-density gas ($n_{\text{crit}} \sim 10^5$ cm$^{-3}$).

In contrast to HCN and CS, CN 1-0 emission is associated more closely with the positions of protostars and the continuum
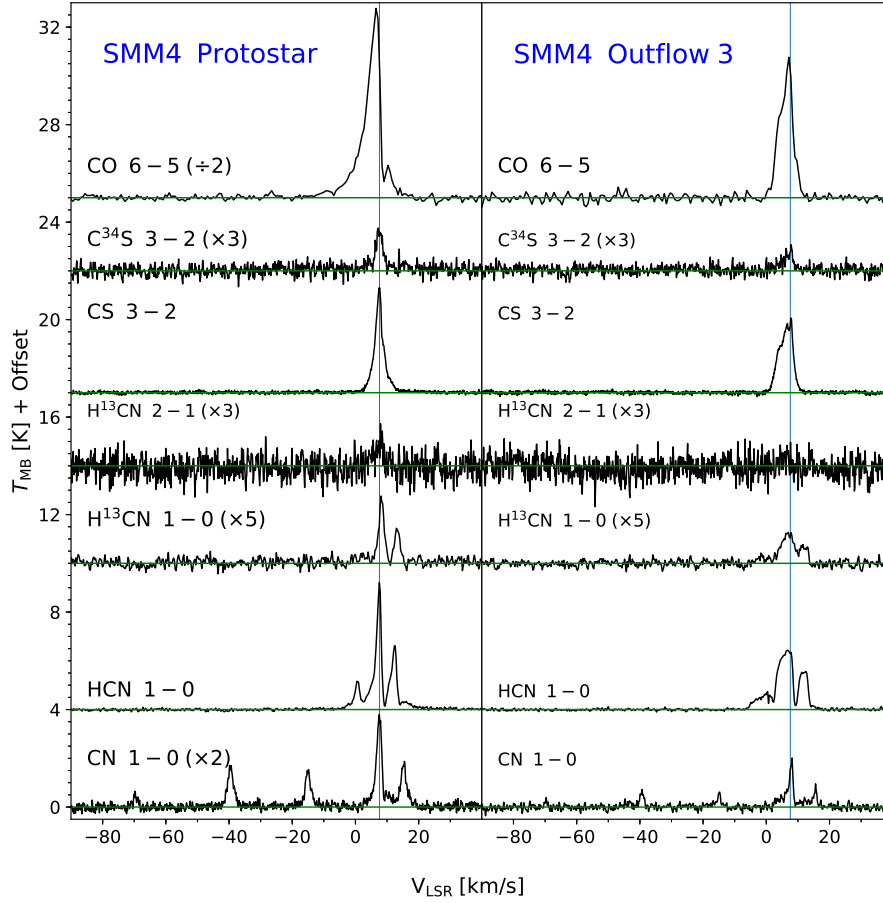
Fig. 3: Line profiles of CO 6-5, $C^{34}S$ 3-2, CS $J = 3 - 2$, $H^{13}CN$ 1-0, HCN 1-0 and CN 1-0 lines at the protostar position Ser SMM4 (left) and the associated outflow position nr 3, see Table 3 (right). Spectra of CO 6-5, $C^{34}S$ 3-2, $H^{13}CN$ and CN are scaled in flux by a factor of 0.5, 3, 5 and 2, respectively. **The $H^{13}CN$ $J = 2 - 1$ line is not detected in the outflow position**.

Table 3: Molecular line ratios of the fully integrated line profile and the line wings

| Source | CN / HCN | | CS / CO | | HCN / CO | | HCN / $H^{13}CN$ | | CS / $C^{34}S$ | $H^{13}CN$ 2-1/1-0 |
|---|---|---|---|---|---|---|---|---|---|---|
| | Full | Line wings | Full | Line wings | Full | Line wings | Full | Line wings | Full | Full |
| Protostar positions | | | | | | | | | | |
| Ser SMM1 | 0.61 | 0.40 | 0.08 | 0.05 | 0.14 | 0.10 | 6.51 | 12.45 | 4.66 | |
| Ser SMM2 | 0.65 | 0.53 | 0.38 | 0.23 | 0.58 | 0.35 | 8.74 | 22.28 | 9.98 | |
| Ser SMM3 | 0.85 | 0.57 | 0.16 | 0.10 | 0.27 | 0.10 | 25.99 | 42.90 | 16.50 | |
| Ser SMM4 | 0.47 | 0.40 | 0.16 | 0.12 | 0.23 | 0.13 | 13.43 | 14.91 | 9.88 | 1.98 |
| Ser SMM5 | 0.67 | 0.31 | 0.19 | 0.09 | 0.31 | 0.17 | 5.26 | | 7.95 | |
| Ser SMM6 | 0.81 | 0.55 | 0.29 | 0.19 | 0.44 | 0.14 | 15.10 | 17.39 | 11.19 | |
| Ser SMM8 | 0.43 | 0.27 | | | | | 49.39 | 117.19 | 17.57 | |
| Ser SMM9 | 0.24 | 0.11 | 0.34 | 0.30 | 0.57 | 0.49 | 8.73 | 16.33 | 6.78 | 1.31 |
| Ser SMM10 | 0.41 | 0.15 | 0.14 | 0.09 | 0.29 | 0.23 | 7.00 | 31.11 | 9.12 | |
| Ser SMM12 | 0.71 | 0.63 | 0.57 | 0.40 | 0.82 | 0.49 | 8.84 | 10.82 | 17.70 | |
| Outflow positions | | | | | | | | | | |
| 1 (-11.00,33.00) | 0.58 | 0.24 | 0.24 | 0.15 | 0.43 | 0.31 | 9.87 | | 4.16 | |
| 2 (114.86,-153.00) | 0.51 | 0.47 | 0.35 | 0.24 | 0.47 | 0.27 | 13.48 | 27.12 | 10.71 | |
| 3 (56.00,-112.00) | 0.13 | 0.03 | 0.54 | 0.56 | 0.74 | 0.72 | 11.92 | 12.29 | 15.57 | |
| 4 (-54.00,81.00) | 0.25 | 0.13 | 0.63 | 0.54 | 0.97 | 0.84 | 8.38 | 12.12 | 8.90 | |
| 5 (138.86,-162.60) | 0.56 | 0.49 | 0.26 | 0.18 | 0.36 | 0.21 | 9.05 | 11.52 | 9.76 | |

Sources in the upper part of the table refer to the positions of protostars within the IRAM maps (Figure 1 and 2), positions in the lower part refer to selected outflow positions on the same maps. Coordinates of the outflow positions refer to J2000 RA 18:29:49.6 and DEC 01:15:20.5. The ranges adopted to calculate the emission in line wings are **determined at 3 $\sigma$ level for each molecule and position separately. The inner velocity range was calculated based on the $C^{18}O$ 6-5 profile.**.

peaks at 250 $\mu$m, and not the outflows (Figures 1 and 2). The emission is the strongest at Ser SMM4, SMM3, and SMM6, and the region in between these three protostars. The differences in spatial extent between CN and the outflow tracers suggest a different physical origin (see §5).

### 3.2. Detection rates and line profiles

To explore gas properties in Serpens, we selected 10 protostar positions and 5 outflow positions for more in-depth analysis (see Tables 1 and 2, and Figure 2). Figure shows line profiles of targeted species and transitions toward Ser SMM4 and its outflow. Appendix C shows the line profiles at each selected position and the table with line fluxes.

All targeted species and their isotopologues were detected in the each and every position of the protostars in Serpens , **except the H$^{13}$CN 2-1 which was detected in two positions only (Ser SMM4 and Ser SMM9). Due to different datasets Ser SMM8 protostar was not covered by CO observations. del: In contrast** Emission in the outflow positions was commonly detected **del: only** in HCN **del: (5/5)**, CS **del: (5/5)**, CN and CO **del: (5/5)**. **(Detections in the targeted lines isotopologues were seen in C$^{34}$S 3-2 , H$^{13}$CN 1-0, but not in H$^{13}$CN 2-1**. In case of HCN and CN, up to 3 and 5 components are detected as the result of the hyperfine splitting, respectively.

The line shapes at both protostar and outflow positions show a relatively broad profiles, with outflow wings in CS extending of **13.6** km s$^{-1}$ and **9.8** km s$^{-1}$ at Ser SMM4 source and outflow, respectively (Figure 3.2). Clearly, the beam sizes of IRAM encompass a substantial amount of outflow emission even at the protostar position.

In order to quantify the emission in the line wings, we use the line profile of C$^{18}$O **6-5** for Ser SMM1 **TBC ??**, which is a good envelope tracer. The profile extends from 7.8 km s$^{-1}$ to 9.4 km s$^{-1}$ - the velocity ranges we exclude for the intensity integration of our line profiles. The outer velocity ranges for each of the profiles are calculated for each line separately based on the measured rms and the 2 $\sigma$ signal. Appendix D shows the table with calculated intensities in the line wings for all selected positions.

In case of Ser SMM4 (Figure 3.2), the emission in the line wings of CS 3-2 is **61**% of the total profile in the protostar position and **72**% in the outflow position. Similar characteristics is seen in HCN line wings (**48**% and **68**%, respectively). In contrast, CN 1-0 is detected mostly at source velocity, with only **40**% of emission in the line wings. Among all 15 positions, exceptionally broad line wings in HCN and CS are detected in the Ser SMM1, Ser SMM9 and Ser SMM10 protostar positions and outflow positions nr 1, 4, and 5 (Table 3) **, exceeding 70% of the total profile in HCN and 58% in CS.**

The shapes of line profiles clearly indicate that the emission in various species is detected in different physical components of the protostellar systems. For the sake of our forthcoming analysis, we will consider the emission in the line wings alone and in the fully integrated profiles separately.

### 3.3. Line ratios

Table 3 shows the molecular line ratios at protostar and outflow positions in Serpens calculated separately for the fully integrated profiles and for the line wings. Here, we will discuss the results for (i) ratios of different isotopologues, informing about the line opacities, (ii) the ratio of two transitions of H$^{13}$CN, indicating
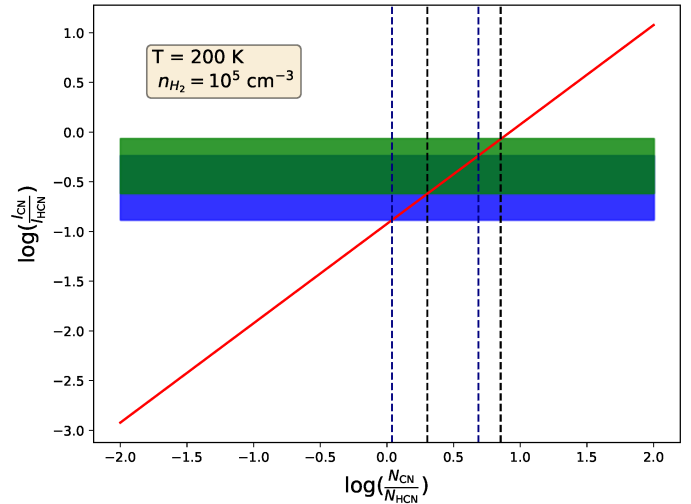
Fig. 4: The ratio of CN and HCN column densities obtained with RADEX for $n_{\rm H} = 10^5$ cm$^{-3}$ and $T_{\rm kin} = 200$ K (red line). The observed line intensity ratio is shown as a rectangle, with green color corresponding to the values observed at the protostar position and blue color for the outflow positions. **Column density ranges are marked with black and navy dashed lines for protostars and outflow positions, respectively.**

Table 4: **Model-dependent column density ratios of CN and HCN**

| $n_{\rm H_2}$ (cm$^{-3}$) | $T_{\rm kin}$ (K) | $\log_{10}(N(CN)/N(HCN))$ protostars | $\log_{10}(N(CN)/N(HCN))$ outflows |
|---|---|---|---|
| $10^4$ | 30 | 0.24-0.79 | -0.02-0.63 |
| $10^4$ | 75 | 0.16-0.71 | -0.10-0.55 |
| $10^4$ | 200 | 0.12-0.67 | -0.14-0.51 |
| $10^5$ | 30 | 0.28-0.83 | 0.016-0.67 |
| $10^5$ | 75 | 0.27-0.82 | 0.00-0.65 |
| $10^5$ | 200 | 0.30-0.85 | 0.04-0.69 |
| $10^6$ | 30 | 0.38-0.92 | 0.10-0.75 |
| $10^6$ | 75 | 0.43-0.98 | 0.16-0.81 |
| $10^6$ | 200 | 0.50-1.05 | 0.23-0.88 |

gas temperature, (iii) ratios of different species, reflecting their relative abundances.

#### 3.3.1. Ratios of different isotopologues

**To be re-written after the table is ready** The line ratio of the same transition of two isotopologues can be used a tracer of line opacity of the more abundant species, assuming that the emission in the other isotopologue is optically thin. We adopt a standard method described in (Goldsmith et al. 1984) to determine the line opacities of HCN 1-0 and CS 3-2 lines, both in the protostar and outflow positions (**TBC**). We assume that both isotopologues arise from the same physical region, described by the excitation temperature, $T_{\rm exc}$, and in local thermodynamical equilibrium (LTE). Using the equation 1, we obtain the values of **0.3-5.7** and **0.3-4.8** for the fully-integrated line profiles **of HCN**

**and CS with their isotopologues respectively**.

$$\frac{T_{\text{HCN}}}{T_{\text{H}^{13}\text{CN}}} = \frac{X[\text{HCN}]}{X[\text{H}^{13}\text{CN}]} \frac{1 - \exp(-\tau_{\text{HCN}})}{\tau_{\text{HCN}}} \tag{1}$$

For comparison, the expected ratio in case of optically emission is 30 and **20** for the HCN/H$^{13}$CN (Daniel et al. 2013) and CS/C$^{34}$S (**Tercero et al. 2010**) ratios, respectively. Thus, the emission in both species is optically thick, when the entire profile is considered. In contrast, the ratios **optical depths?** of **0.6-1.8** and YYY measured in the line wings are comparable (?) to the optically thin ratio. Thus, in the selected velocity ranges the ratios of line emission is these species are a valuable measure of real emission.

We note that an alternative method of calculating the line optical depths is to check the ratios of various components due to hyperfine splitting. However, for HCN show considerable anomalies ((**Loughnane et al. 2012). The method can be applied to CN molecular lines based on three the strongest components F=3/2→1/2, F=5/2→3/2, F=1/2→1/2 with ratio of 0.1235:0.3333:0.0988 (Skatrud et al. 1983). The optical depth varies from 0.4 to 1.6 and from 0.2 to 1.0 for protostars and outflows positions, respectively.**

The calculated optical depths are in agreement with the calculations performed using the 1D radiative-transfer code RADEX (van der Tak et al. 2007). Assuming column density of HCN of $3 \times 10^{14}$ cm$^{-2}$, hydrogen density of $10^5$ cm$^{-3}$ and kinetic temperature of the gas of 50 K, the optical depths of HCN **is 4.4**. For CS, the **value is 2.1, assuming column density of $5 \times 10^{13}$ cm$^{-2}$.**

### 3.3.2. The H$^{13}$CN 2-1/1-0 ratio

**The H$^{13}$CN 2-1 emission was detected in two positions only: Ser-SMM4 and Ser-SMM9. The ratio of two lowest transitions is 1.98 and 1.31 respectively. Based on two different transitions of the same molecule, the exitacion temperature can be calculated (Kristensen et al. 2003):**

$$T_{\text{ex}} = \frac{E_u - E_l}{k \ln \frac{n_l}{n_u}} \tag{2}$$

**where $E_i$ refers to energy and $n_i$ refers to population of upper and lower level. The exitation temperature equals 2.43 K and 2.77 K for Ser-SMM4 and Ser-SMM9 respectively.**

### 3.3.3. Ratios of different species

**To be re-written after the table is ready** The median value of the CN/HCN ratio at the protostars positions is $0.63 \pm 0.19$. Slightly lower ratio was calculated for the outflow positions with a similar standard devation ($0.51 \pm 0.20$). The CN/HCN ratio varies between 0.13 at the Outflow 3 to 0.85 at the Ser-SMM3.

There is no significant dependence between the CN/HCN ratio and the evolutionary stage of a source, although the Class I protostars have statistically higher CN/HCN ratio than the Class 0 YSOs ($0.67 \pm 0.17$ and $0.61 \pm 0.23$ respectively).

## 4. Analysis

In this section, we calculate column densities of the molecules with the aid of radiative-code RADEX and compare them to the results from the chemical-code Nahoon, run for a set of gas temperatures, densities and UV radiation fields.

### 4.1. Column densities of molecules from observations

In case of optically thin lines and the LTE conditions, the column density of the upper level of a given molecule, $N_u$, can be calculated using the equation 2. Here, $\beta$ is a constant equal 1937 cm$^{-2}$, $W$ is the integrated intensity of the emission line ($\int T_{mb} dV$), and $\nu$ is a transition frequency in GHz.

In order to calculate the total column density of a given molecule, we need to know the temperature of the gas. We will assume $T_{\text{ex}}$ of 75 K, which is a typical temperature in low-mass protostars (**Yıldız et al. 2015), refer to the value determine from H13CN**. Equation 4 takes into account the temperature-dependent partition function $Q(T)$ for a given molecule, and the upper level energies ($E_u$) and level degeneracies ($g_u$); $k$ is a Boltzmann constant. Appendix E shows the results obtained for all observed molecules, both for the fully-integrated line profiles and the lines wings.

$$N_u = \beta \frac{\nu W}{A} \tag{3}$$

$$N_{\text{tot}} = Q(T_{\text{exc}}) \exp(\frac{E_u}{k T_{\text{exc}}}) \frac{N_u}{g_u} \tag{4}$$

Because of the optical thickness of HCN (§3), we also employ the non-LTE radiative transfer code RADEX to obtain independent determinations of the column densities. In order to mimic the optically thin case, for the calculations we adopt the HCN column density of $10^8$ cm$^{-2}$. We vary the column density of CN from $10^6$ cm$^{-2}$ to $10^{10}$ cm$^{-2}$. The typical physical conditions of the gas in low-mass star forming regions are: number densities, $n_H$ of the order of $10^4 - 10^6$ cm$^{-1}$ and kinetic temperature $T_{\text{kin}}$ of 30-200 K. Table 4 shows the ratios of the calculated column densities of CN and HCN for these different sets of parameters, and assuming a line width of $1.0$ km s$^{-1}$ **for protostars positions and outflows separately.**

The models are a means to translate the observed line ratios of CN and HCN into column densities ratios. Figure 4 show the model calculated for the densities and temperatures typical for outflows in low-mass protostars (**van Kempen et al. 2009, Dionatos et al. 2013**). The observed line intensity ratio (full profile) in logarithm is in the range from **-0.62 to -0.07 and from -0.87 to -0.24 for protostars and outflow positions, respectively. The corresponding column density ratio is in the range 0.12 to 1.05 and -0.14 to 0.88**. Similar models were calculated for other sets of temperatures and densities, and the determined scaling factors between the intensity and column density ratios show a very weak dependence on the adopted physical parameters. The resulting column density ratios of CN and HCN are **in order of 1-10. del: , respectively.**

### 4.2. Theoretical column densities from Nahoon

The Nahoon chemical code is used to calculate theoretical column densities of molecules for a set of physical conditions and UV field strengths; it is a well-known purely gas-phase chemical code for astronomical applications (Wakelam et al. 2012).

The Nahoon solver computes the chemical evolution in time including 489 species and 6992 gas-phase and gas-grain reactions based on rate coefficients from the Kinetic Database for Astrochemistry (KIDA) database[2]. The Nahoon code can model chemistry at a fixed temperature and density (0D modeling), as

---

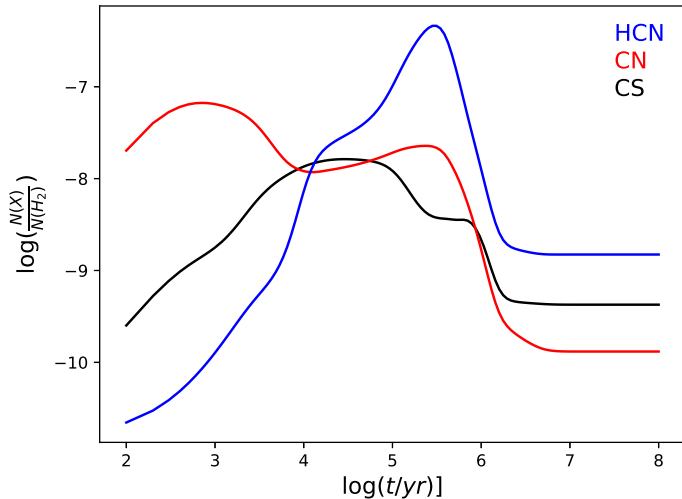[2] http://kida.obs.u-bordeaux1.fr/

Fig. 5: Time evolution of CN (red line), HCN (blue line) and CS (black line) abundances obtained with Nohoon astrochemical code with initial parameters of $n_H = 10^4$ cm$^{-3}$, $T = 10$ K, $A_V = 5$ mag. The assumed cosmic-ray ionization rate is $1.3 \times 10^{17}$ s$^{-1}$, dust to gas mass ratio is 0.01, dust grain radius is $10^{-5}$ cm, grain density is 3 g cm$^{-3}$.
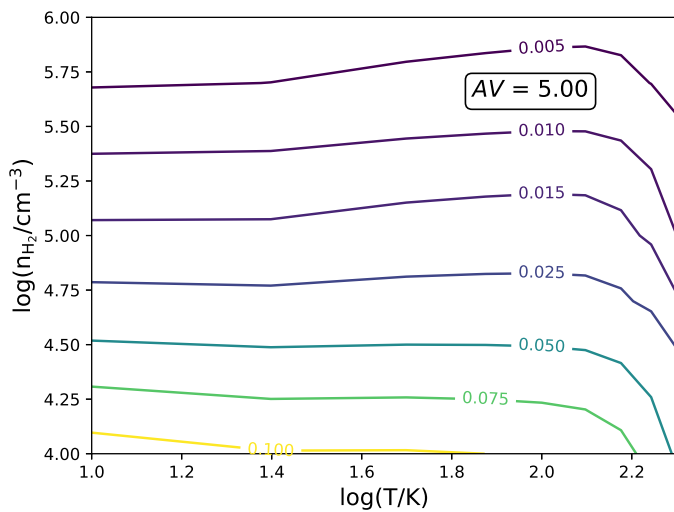


Fig. 6: Contour plot of Nahoon sets of models of CN/HCN abundances ratio with fixed visual extinction $A_V = 5$ mag at the time of $10^7$ yrs after star formation began in the cloud.

well as at grid of temperature, density and visual extinction (1D modeling).

The UV radiation in Nahoon is described through the relation between visual extinction $A_V$ and the photodissociation rate coefficient $k$ (equation 4). Here, $\alpha$ and $\gamma$ are coefficients of photodissociation of HCN equal to $1.64 \times 10^{-9}$ and 3.12, respectively ((Heays et al. 2017)).

$$k = \alpha e^{-\gamma A_V} \qquad (5)$$

In our analysis, we calculate 1D grid with the latest version of Nahoon code (Nahoon_kida.uva.2014). The evolution of
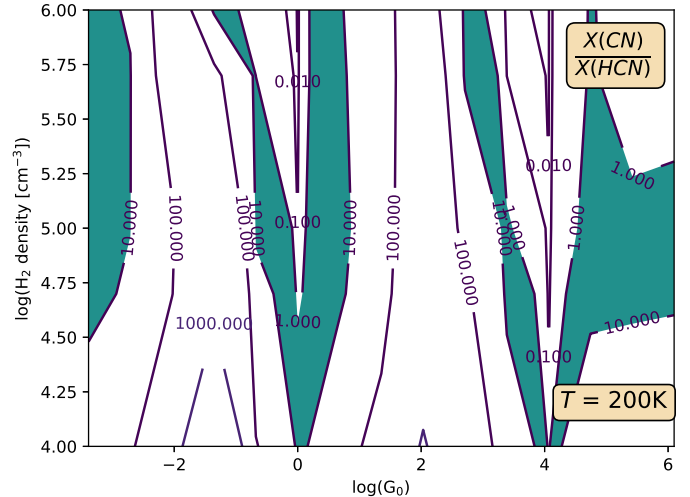


Fig. 7: The column ratio of CN and HCN from Nahoon for a range of hydrogen densities and UV field strengths assuming $T$ equal 200 K (contours) and the observed column density ratios (in green).

the chemical network starts at the time of a dense cloud formation. Figure 5) shows a model corresponding to a typical dense cloud with temperature of 10 K and hydrogen total density of $n_H = 10^4$ cm$^{-3}$. The chemical composition of the CN, HCN and CS molecules becomes stable at the time of $10^7$ yrs; the HCN abundance is higher than that of CN. We assume the time of $10^6$ yrs as the moment when the star formation starts in a dense cloud. We use model abundances for all 489 species at this moment of time as an input data for the forthcoming set of models.

The closest neighbourhood of low-mass protostars is simulated based on the initial abundances of all species from starless cloud modelling. We adopt the cosmic-ray ionization rate of $1.3 \times 10^{17}$ s$^{-1}$ (**Cravens & Dalgarno 1978**). The sets of models are run for the temperature range between 10 and 200 K and the total hydrogen densities from $10^4$ cm$^{-3}$ to $10^6$ cm$^{-3}$.

Figure 6 show the model results assuming visual extinction of 5 mag and lack of UV radiation. In that case, HCN is more abundant than CN by about 2-3 orders of magnitude. The column density ratio of CN and HCN weakly depends on the gas temperature; we fix the gas temperature at 200 K.

In the next step, we run the model for the range of visual extinction between $-4.5^m$ and $2.5^m$ that corresponds to the UV radiation field $G_0$ of $4 \times 10^{-4}$ to $1.25 \times 10^6$. Figure 7 shows the ratio of CN and HCN as a function of $n_H$ and $G_0$. The observed ratios of 1-10 match the calculated ratios for the relatively weak UV fields of $10^{-1} - 10^1$.

## 5. Discussion

### 5.1. Comparison of the spatial extent of CN and HCN

The relative abundance of CN and HCN molecules is widely used a tracer of UV radiation in different astronomical context: reflection nebulae (e.g. Fuente et al. 1995), proto-planetary disks (e.g. Chapillon et al. 2012), proto-brown dwarfs (e.g. Riaz et al. 2018). CN is a product of photodissociation of HCN with the photodissociation rate of $1.64 \times 10^{-9}$. CN has smaller photodissociation rate of $5.19 \times 10^{-10}$ (Heays et al. 2017), thus is not
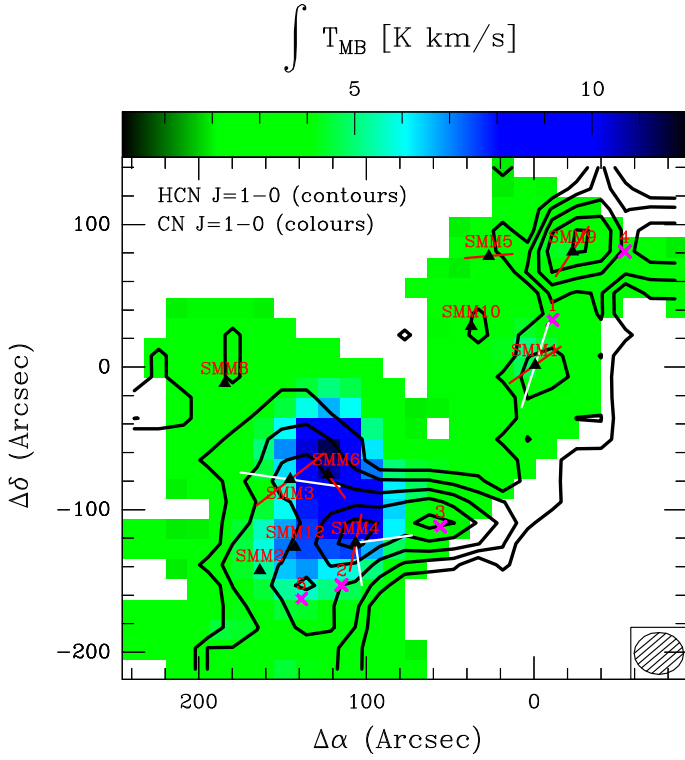
Fig. 8: Map of the intensity ratio of CN 1-0 (colours) and HCN 1-0 (contours) in Serpens. The labels are the same as in Figure 2. **comment on contours** The CN emission has been resampled to beam size of HCN in order to compare the same emitting regions.



Fig. 9: Reactions network for UV irradiated gas of $G_0 = 10^{-1} - 10^1$).



Fig. 10: Dominant reactions of HCN destruction. Reactions contributed at least 50% of total flux are marked with full colous. Transparent colours correspond to 30%-50% contribution.

that sensitive for photodissociation as HCN. Since CN and HCN can be photodissociated selectively, therefore the CN/HCN ratio probes regions affected by UV radiation. The ratio is the highest near the source of the UV emission, and decreases with the distance from the source (Fuente et al. 1993).

Figure 8 shows a large-scale map of CN 1-0 and HCN 1-0.

The CN $J = 1 - 0$ transition is shifted to the north in respect to the HCN $J = 1 - 0$ emission. It is highly concentrated in the SE subcluster, while the NW subcluster is dominated ny the HCN. Both molecules show a diffusive 'bridge' between the two subclusters. It is connected with Ser-SMM4 and Ser-SMM1 outflows in HCN, while the CN follows the dust continuum emission. The emission in both molecules is anti-corelated north from Ser-SMM6 and west from Ser-SMM4 sources. At the dense area of Ser-SMM9 surrounding CN/HCN ratio is significantly weaker.

Both species has been detected in all sources positions. CN as a product of HCN photodissotiation indicates other properties of low-mass protostars surroundings (Section 4). The highest CN/HCN integrated intensity ratio occurs in Ser-SMM6 and Ser-SMM3 protostars, as well as in the outflow position no. 5. On the other hand, Ser-SMM9 object is characterised by very low CN/HCN line ratio. Similarly low CN/HCN ratio is measured in outflow positions no. 3 and 4.

Most of the sources show high flux values in both molecules (Table 3). However, they present unequal levels which indicates regions of different properties. The CN/HCN ratio varies between protostars positions, as well as between off-source positions. The highest CN/HCN ratio is found in Ser-SMM3, Ser-SMM6 and Ser-SMM8 sources. This parameter seems to be
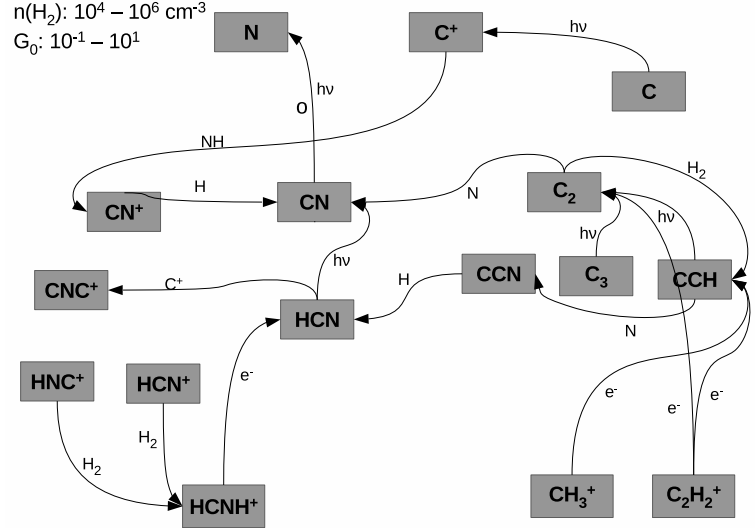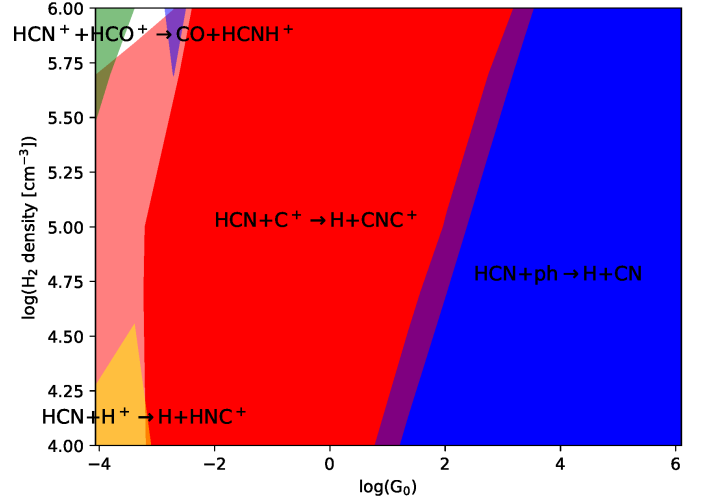
not correlated with the evolutional stage of a protostar. All the sources with the highest CN/HCN ratio are located in the SE subcluster. Ser-SMM3 and Ser-SMM6 are situated in close neighbourhood, in the area characterised by high emission of CN $J = 1 - 0$ line. At Ser-SMM9 and Ser-SMM10 protostars the lowest CN/HCN ratio is observed. Both sources are young, Class 0 YSOs. In addition they are separated by $\approx 45$ arcsec from the other sources.

## 5.2. UV field strengths in Serpens

Low CN/HCN ratio found in astrochemical model for strongly irradiated gas is a surprising result. Both production and destruction of each molecule need to be investigated in order to explain

Table 5: Dominant processes in CN and HCN chemistry at 50 K

| Molecule | Weak UV fields ($G_0 = 10^{-3} - 10^{-1}$) | Medium UV fields ($G_0 = 10^{-1} - 10^{1}$) | Strong UV fields ($G_0 = 10^{1} - 10^{6}$) |
|---|---|---|---|
| | **Destruction** | | |
| | $O + CN \rightarrow N + CO$ | $CN + ph \rightarrow C + N$ | $CN + ph \rightarrow C + N$ |
| | $CN + N \rightarrow C + N_2$ | $O + CN \rightarrow N + CO$ | |
| CN | **Production** | | |
| | $N + CH \rightarrow H + CN$ | $N + C_2 \rightarrow C + CN$ | $HCN^+ + e^- \rightarrow H + CN$ |
| | $CNC^+ + e^- \rightarrow C + CN$ | $H + CN^+ \rightarrow CN + H^+$ | $N + CH \rightarrow H + CN$ |
| | $N + C_2 \rightarrow C + CN$ | | $H + CN^+ \rightarrow CN + H^+$ |
| | | | $N + C_2 \rightarrow C + CN$ |
| | **Destruction** | | |
| | $HCN + C^+ \rightarrow H + CNC^+$ | $HCN + C^+ \rightarrow H + CNC^+$ | $HCN + ph \rightarrow H + CN$ |
| | $HCN^+ + HCO^+ \rightarrow CO + HCNH^+$ | $HCN + ph \rightarrow H + CN$ | $HCN + C^+ \rightarrow H + CNC^+$ |
| | $HCN + H^+ \rightarrow H + HNC^+$ | | |
| HCN | $HCN + ph \rightarrow H + CN$ | | |
| | **Production** | | |
| | $N + CH_2 \rightarrow H + HCN$ | $H + CCN \rightarrow C + HCN$ | $HCNH^+ + e^- \rightarrow H + HCN$ |
| | $H + CCN \rightarrow C + HCN$ | $HCNH^+ + e^- \rightarrow H + HCN$ | $H + CCN \rightarrow C + HCN$ |
| | $HCNH^+ + e^- \rightarrow H + HCN$ | | |
| | $C + HNC \rightarrow C + HCN$ | | |

the reason behind HCN abundances being higher than expected. Detailed models of the most dominant reactions for destruction and production of each molecule are presented in Fig. G.1 – Fig. G.3 with the assumption of fixed 50 K temperature. Reaction flux is defined as reactants abundances multiplied by reaction rate coefficient. Only these reactions were taken into consideration which accumulated flux is greater than 80% of the total flux of all reactions contributed in the studied molecules destruction or production.

The reactions distribution in the parameter space is not very strongly depended on hydrogen densities. The strength of an additional UV radiation source is the parameter that distinguishes the dominant reactions the most. It was divided into three regimes: with weak, intermediate and strong UV field. The reactions where CN or HCN production or destruction is greater than 30% are listed in Tab. G.1 as well as illustrated in Fig. G.4-Fig. G.5.

In the regime of weak UV radiation fields dominant formation channels of CN and HCN are hydrocarbons (CH and $CH_2$ respectively) reactions with atomic nitrogen. In more dense areas electron reaction with CNC cation plays role in the CN formation. The destruction of CN is mostly dominated with reaction with neutral oxygen (60-70%) or nitrogen (30% or less). In weakly irradiated environment atomic elements are more abundant in the neutral state. More of the ionised atoms are produced with the increase of the UV radiation what blocks these effective channels of CN destruction.

On the other hand, HCN destruction is driven by many channels in the weakest UV regime. Simultaneous impact of few different reactions is not as effective as the reaction ruling the CN destruction. It leads to higher HCN abundances compared to CN. HCN reaction with abundant C+ is the dominant destructive reaction for slightly stronger radiation fields ($>10^{-3}$). This reaction results in CNC+ production which quickly reacts with electron forming CN. That explains why CN/HCN ratio increases with larger radiation.

CN/HCN ratio is widely used as UV radiation tracer in PDRs (eg. Thi et al. 2004, Han et al. 2015). HCN photodissociates into CN molecule and H atom, while CN requires more energetic photon (> 12.4 eV) to be disintegrated (van Dishoeck 1987). This leads to higher abundance of CN molecules and increases CN/HCN column density ratio. Fluxes of HCN photodissociation (Fig. 10) show that this reaction has marginal contribution in nitrogen chemistry up to $G_0 \approx 100$.

### 5.3. Comparisons to the results from Herschel

Previous studies of energetic processes around low-mass protostars showed observational premises of the influence of UV radiation on molecules. These works focused on intermediate-*J* CO transitions (up to 6-5) that traces gas with the kinetic temperature around 100 K. With the Water in Star-Forming Regions with the Herschel Space Observatory (WISH) project (van Dishoeck et al. 2011b) higher CO rotational transitions (up to 49-48) were studied that provided information of two temperature components seen in molecular outflows: warm with $T_{rot} \approx 300$ K and hot with $T_{rot} \approx 600 - 800$ K (Karska et al. 2013, Green et al. 2013). The observations of the water molecule shows a broad and medium-broad components associated with non-dissociative *C* shocks and dissociative *J* shocks respectively (Kristensen et al. 2013, Mottram et al. 2014). These spectral components can be correlated to the CO rotational temperature components (Kristensen et al. 2017). Another tracers sensitive to UV radiation, ionised hydrides such as $CH^+$, $OH^+$ and $H_2O^+$, were found in outflow cavities (Benz et al. 2016). The UV fluxes were estimated as $10^2$-$10^3$ higher than average interstellar radiation. There is no molecular evidence for influence of X-rays for chemical compositions of low-mass protostars.

Most of the low-mass protostars have a broad, centered on $v_{source}$ CO $J = 16 - 15$ and $H_2O$ component in their spectra (Kristensen et al. 2017). There are typically $\approx 20$ km s$^{-1}$ broad and associated with cavity shocks. The emitting gas is located in shocks along the outflow cavity wall or along the molecular wind alternatively (Yvart et al. 2016). Some of the sources show a narrow, offset component as well that is seen in the PACS CO ladder with $T_{rot} \approx 600 - 800$. The gas dissociated by UV photons and carried out form the protostar was proposed as an origin of the pre-shock gas (Kristensen et al. 2017). Thus, ultra-

violet radiation can propagate in large scales of 1000 AU from the central protostar, changing the properties of the surrounding matter. The hypothesis of the UV irradiated shocks is raised also based on $H_2O$/OH ratio observations. The ratio showed a few orders of magnitude disagreement with fully-shielded shock models (Karska et al. 2014). The observations are reproduced with predictions of *C*-shock models illuminated by UV photons of the strength 0.1-10 times the interstellar value (Melnick & Kaufman 2015). The other photodissociation tracers, fluxes of [OI] and [CII] are significantly higher than predicted by fully-shielded *C*-shock models (Karska et al. 2018). Therefore, ultraviolet radiation may play an important role in low-mass protostars surroundings.

## 6. Conclusions

IRAM 30 m / EMIR observations of CN and HCN emission pinpoint the location of the impact of UV radiation on the chemistry of low-mass star forming region in Serpens. A combination of simple models using radiative-code RADEX and chemical code Nahoon allows us to determine physical conditions of the gas, column densities of molecular species, and estimate the UV radiation field strength. The main conclusions of our study are the following.

– The spatial extent of HCN 1-0 and CN 1-0 show significant differences, with HCN resembling the CO 6-5 emission tracing outflows and CN concentrated close to the individual protostar positions or their groups.

– The ratios of CN and HCN systematically differ between protostar and outflow position, both taking into account the integrated line profile and the line wings **[TBC!]**. The ratio is the highest at the positions of the protostars, confirming the impact of UV identified using *Herschel* as part of the WISH program.

– For typical densities of low-mass protostellar envelopes of $10^5$ cm$^{-3}$ and gas temperatures of 75 K **(TBC)**, the chemical network for nitrogen-species is sensitive to UV photons. The ratio of CN and HCN is primarily driven by the UV photodissociation of HCN into CN in a broad range of UV field strength. The tracer is most useful for $G_0 > 10^2$.

– The column density ratios of CN and HCN equals 1-10, which corresponds to $G_0 \approx 10^{-2}$. These values are in agreement with, yet in the lower end of the UV field strength obtained using $H_2O$ and OH ratios from *Herschel*.

Similar observations for a larger sample of sources is needed to fully exploit the impact of UV radiation on the physical and chemical conditions in low-mass star forming regions. Detailed 3D modelling of protostellar envelopes with outflow cavities is necessary to fully constrain the strengths of the UV fields in physical components of young stellar objects.

## References

André, P., Men'shchikov, A., Bontemps, S., et al. 2010, A&A, 518, L102
Bachiller, R., Pérez Gutiérrez, M., Kumar, M. S. N., & Tafalla, M. 2001, A&A, 372, 899
Benz, A. O., Bruderer, S., van Dishoeck, E. F., et al. 2016, A&A, 590, A105
Bruderer, S., Benz, A. O., Doty, S. D., van Dishoeck, E. F., & Bourke, T. L. 2009, ApJ, 700, 872
Casali, M. M., Eiroa, C., & Duncan, W. D. 1993, A&A, 275, 195
Cesaroni, R. 2005, Ap&SS, 295, 5
Chapillon, E., Guilloteau, S., Dutrey, A., Piétu, V., & Guélin, M. 2012, A&A, 537, A60
Cravens, T. E. & Dalgarno, A. 1978, ApJ, 219, 750
Daniel, F., Gérin, M., Roueff, E., et al. 2013, A&A, 560, A3
Davis, C. J., Matthews, H. E., Ray, T. P., Dent, W. R. F., & Richer, J. S. 1999, MNRAS, 309, 141
de Graauw, T., Helmich, F. P., Phillips, T. G., et al. 2010, A&A, 518, L6
Di Francesco, J., Johnstone, D., Kirk, H., MacKenzie, T., & Ledwosinska, E. 2008, ApJS, 175, 277
Dionatos, O., Jørgensen, J. K., Green, J. D., et al. 2013, A&A, 558, A88
Dionatos, O., Nisini, B., Codella, C., & Giannini, T. 2010, A&A, 523, A29
Doty, S. D. & Neufeld, D. A. 1997, ApJ, 489, 122
Dunham, M. M., Allen, L. E., Evans, Neal J., I., et al. 2015, ApJS, 220, 11
Enoch, M. L., Evans, Neal J., I., Sargent, A. I., & Glenn, J. 2009, ApJ, 692, 973
Enoch, M. L., Glenn, J., Evans, Neal J., I., et al. 2007, ApJ, 666, 982
Evans, Neal J., I., Dunham, M. M., Jørgensen, J. K., et al. 2009, ApJS, 181, 321
Frank, A., Ray, T. P., Cabrit, S., et al. 2014, Protostars and Planets VI, University of Arizona Press (2014), eds. H. Beuther, R. Klessen, C. Dullemond, Th. Henning [arXiv:1402.3553]
Fuente, A., Martin-Pintado, J., Cernicharo, J., & Bachiller, R. 1993, A&A, 276, 473
Fuente, A., Martin-Pintado, J., & Gaume, R. 1995, ApJ, 442, L33
Gerin, M., Neufeld, D. A., & Goicoechea, J. R. 2016, ARA&A, 54, 181
Goicoechea, J. R., Cernicharo, J., Karska, A., et al. 2012, A&A, 548, A77
Goldsmith, P. F., Snell, R. L., Hemeon-Heyer, M., & Langer, W. D. 1984, ApJ, 286, 599
Green, J. D., Evans, II, N. J., Jørgensen, J. K., et al. 2013, ApJ, 770, 123
Green, J. D., Yang, Y.-L., Evans, Neal J., I., et al. 2016, AJ, 151, 75
Griffin, M. J., Abergel, A., Abreu, A., et al. 2010, A&A, 518, L3
Güsten, R., Baryshev, A., Bell, A., et al. 2008, Society of Photo-Optical Instrumentation Engineers (SPIE) Conference Series, Vol. 7020, Submillimeter heterodyne arrays for APEX, 702010
Han, X. H., Zhou, J. J., Wang, J. Z., et al. 2015, Astronomy and Astrophysics, 576, A131
Harsono, D., van Dishoeck, E. F., Bruderer, S., Li, Z. Y., & Jørgensen, J. K. 2015, A&A, 577, A22
Harvey, P., Merín, B., Huard, T. L., et al. 2007, ApJ, 663, 1149
Heays, A. N., Bosman, A. D., & van Dishoeck, E. F. 2017, A&A, 602, A105
Herczeg, G. J., Karska, A., Bruderer, S., et al. 2012, A&A, 540, A84
Hurt, R. L. & Barsony, M. 1996, ApJ, 460, L45
Karska, A., Herczeg, G. J., van Dishoeck, E. F., et al. 2013, A&A, 552, A141
Karska, A., Kaufman, M. J., Kristensen, L. E., et al. 2018, ApJS, 235, 30
Karska, A., Kristensen, L. E., van Dishoeck, E. F., et al. 2014, A&A, 572, A9
Kasemann, C., Güsten, R., Heyminck, S., et al. 2006, Society of Photo-Optical Instrumentation Engineers (SPIE) Conference Series, Vol. 6275, CHAMP⁺: a powerful array receiver for APEX, 62750N
Klein, B., Philipp, S. D., Krämer, I., et al. 2006, A&A, 454, L29
Kristensen, L. E., Gustafsson, M., Field, D., et al. 2003, A&A, 412, 727
Kristensen, L. E., van Dishoeck, E. F., Benz, A. O., et al. 2013, A&A, 557, A23
Kristensen, L. E., van Dishoeck, E. F., Mottram, J. C., et al. 2017, A&A, 605, A93
Kristensen, L. E., van Dishoeck, E. F., van Kempen, T. A., et al. 2010, A&A, 516, A57
Kroupa, P. 2002, Science, 295, 82
Lee, K. I., Fernández-López, M., Storm, S., et al. 2014, ApJ, 797, 76
Loughnane, R. M., Redman, M. P., Thompson, M. A., et al. 2012, MNRAS, 420, 1367
Melnick, G. J. & Kaufman, M. J. 2015, ApJ, 806, 227
Mottram, J. C., Kristensen, L. E., van Dishoeck, E. F., et al. 2014, A&A, 572, A21
Myers, P. C. & Ladd, E. F. 1993, ApJ, 413, L47
Neufeld, D. A. & Dalgarno, A. 1989, ApJ, 344, 251
Ortiz-León, G. N., Dzib, S. A., Kounkel, M. A., et al. 2017, ApJ, 834, 143
Ossenkopf, V., Müller, H. S. P., Lis, D. C., et al. 2010, A&A, 518, L111
Pickett, H. M., Poynter, R. L., Cohen, E. A., et al. 1998, J. Quant. Spectr. Rad. Transf., 60, 883
Poglitsch, A., Waelkens, C., Geis, N., et al. 2010, A&A, 518, L2
Riaz, B., Thi, W. F., & Caselli, P. 2018, MNRAS, 481, 4662
Schöier, F. L., van der Tak, F. F. S., van Dishoeck, E. F., & Black, J. H. 2005, A&A, 432, 369

Skatrud, D. D., De Lucia, F. C., Blake, G. A., & Sastry, K. V. L. N. 1983, Journal of Molecular Spectroscopy, 99, 35

Skrutskie, M. F., Cutri, R. M., Stiening, R., et al. 2006, AJ, 131, 1163

Spaans, M., Hogerheijde, M. R., Mundy, L. G., & van Dishoeck, E. F. 1995, ApJ, 455, L167

Stäuber, P., Benz, A. O., Jørgensen, J. K., et al. 2007, A&A, 466, 977

Stäuber, P., Doty, S. D., van Dishoeck, E. F., & Benz, A. O. 2005, A&A, 440, 949

Suresh, A., Dunham, M. M., Arce, H. G., et al. 2016, AJ, 152, 36

Tercero, B., Cernicharo, J., Pardo, J. R., & Goicoechea, J. R. 2010, A&A, 517, A96

Testi, L. & Sargent, A. I. 1998, ApJ, 508, L91

Thi, W. F., van Zadelhoff, G. J., & van Dishoeck, E. F. 2004, Astronomy and Astrophysics, 425, 955

van der Tak, F. F. S., Black, J. H., Schöier, F. L., Jansen, D. J., & van Dishoeck, E. F. 2007, A&A, 468, 627

van Dishoeck, E. F. 1987, in IAU Symposium, Vol. 120, Astrochemistry, ed. M. S. Vardya & S. P. Tarafdar, 51–65

van Dishoeck, E. F., Kristensen, L. E., Benz, A. O., et al. 2011a, PASP, 123, 138

van Dishoeck, E. F., Kristensen, L. E., Benz, A. O., et al. 2011b, PASP, 123, 138

van Kempen, T. A., van Dishoeck, E. F., Güsten, R., et al. 2009, A&A, 507, 1425

Wakelam, V., Herbst, E., Loison, J. C., et al. 2012, ApJS, 199, 21

Walker-Smith, S. L., Richer, J. S., Buckle, J. V., Hatchell, J., & Drabek-Maunder, E. 2014, MNRAS, 440, 3568

Wampfler, S. F., Bruderer, S., Karska, A., et al. 2013, A&A, 552, A56

Wright, E. L., Eisenhardt, P. R. M., Mainzer, A. K., et al. 2010, AJ, 140, 1868

Wyrowski, F., Menten, K. M., Güsten, R., & Belloche, A. 2010, A&A, 518, A26

Yang, Y.-L., Green, J. D., Evans, Neal J., I., et al. 2018, ApJ, 860, 174

Yıldız, U. A., Kristensen, L. E., van Dishoeck, E. F., et al. 2012, A&A, 542, A86

Yıldız, U. A., Kristensen, L. E., van Dishoeck, E. F., et al. 2015, A&A, 576, A109

Yvart, W., Cabrit, S., Pineau des Forêts, G., & Ferreira, J. 2016, A&A, 585, A74

Zinnecker, H. & Yorke, H. W. 2007, ARA&A, 45, 481

## Appendix A: Spectral Energy Distributions

Broad-band observations are needed in order to determine physical properties of a protostar. Dunham et al. 2015 studied properties of protostars in the Serpens molecular cloud using 2MASS (Skrutskie et al. 2006) and Spitzer IRAC/MIPS (Evans et al. 2009), observations covering the range of 1.25–70 $\mu$m, photometry from Wide-field Infrared Survey Explorer 12 and 22 $\mu$m (WISE; Wright et al. 2010), SHARC-II 350 $\mu$m (Suresh et al. 2016), the SCUBA Legacy Catalog 450 and 850 $\mu$m (Di Francesco et al. 2008) and 1.1 mm observations from Bolocam dust survey (Enoch et al. 2007). The Serpens Main region was also observed during the Herschel Gould Belt survey project (André et al. 2010). SPIRE/PACS photometry in the Serpens molecular cloud is discussed in Fiorellino et al. (in prep.).

Based on SEDs the bolometric temperature and luminosity can be calculated for each of the observed protostars. The bolometric luminosity was determined by integrating the SEDs over frequency:

$$L_{bol} = \pi d^2 \int F_\nu d\nu \qquad (A.1)$$

where $d$ is the cloud distance of 436 ± 9.2 pc (Ortiz-León et al. 2017). The bolometric temperature was calculating as described in Myers & Ladd 1993:

$$T_{bol} = 1.25 \, 10^{-11} \, \bar{\nu} \qquad (A.2)$$

where $\bar{\nu}$ is the mean frequency given by:

$$\bar{\nu} = \frac{\int \nu F_\nu d\nu}{\int F_\nu d\nu} \qquad (A.3)$$

Using Scipy *splrep* and *splev* functions cubic smooth spline interpolation of the photometric data was performed while calculating the protostars parameters. Integration along the resulting axis was obtain with the composite trapezoidal rule (*Scipy* package). The photometric data allows us to perform the integration along wide range of wavelength with exception of SMM8. Here we have only 4 photometric points from the Herschel Gould Belt so the calculated bolometric luminosity and temperature can be underestimated.

## Appendix B: Maps in additional tracers

## Appendix C: Molecular line profiles

## Appendix D: Line fluxes

## Appendix E: Observed column densities

## Appendix F: RADEX models
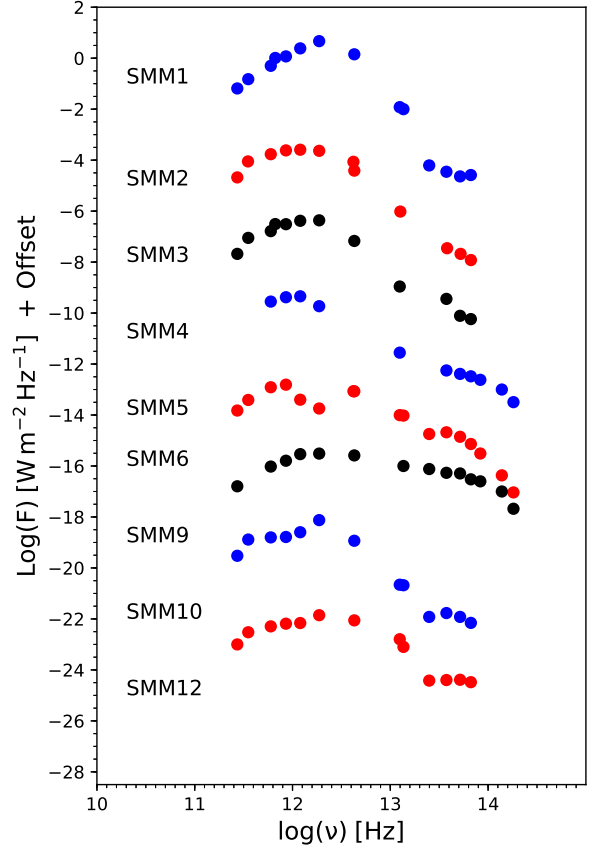
## Appendix G: Dominant reactions in CN, HCN chemistry



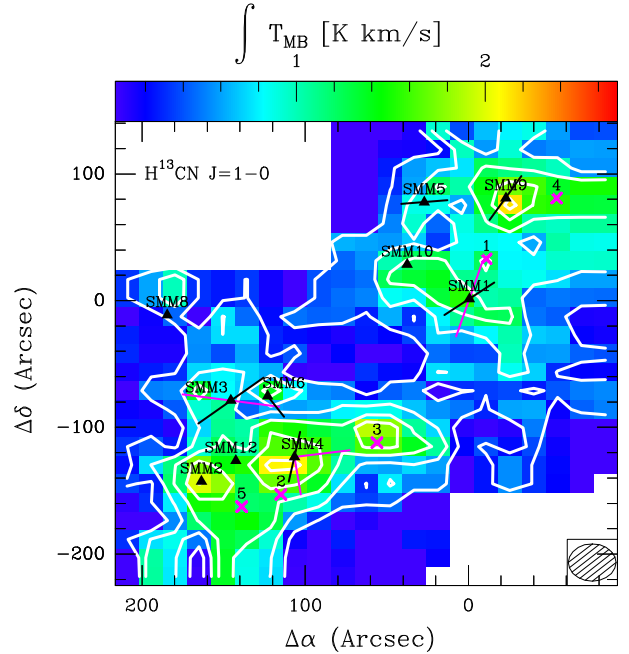Fig. A.1: Spectral Energy Distributions of protostars in the Serpens Main region.



Fig. B.1: Similar to Fig. 2 but the emission of the H$^{13}$CN $J = 1 - 0$ line. The first contour at 10 $\sigma$ level, with step of 10 $\sigma$

Table D.1: Integrated fluxes of the observed line at the positions of protostars

| Source | Line | $\int T_{mb}\,dV$ (K km/s) | $T_{peak}$ (K) | $N_{up}$ (cm$^{-2}$) | $N_{tot}$ (cm$^{-2}$) |
|---|---|---|---|---|---|
| | CN 1-0 | 6.29 | 0.89 | $1.3\times10^{13}$ | $7.9\times10^{14}$ |
| | HCN 1-0 | 10.34 | 1.76 | $6.5\times10^{12}$ | $2.5\times10^{14}$ |
| SMM1 | CS 3-2 | 5.89 | 1.57 | $4.1\times10^{12}$ | $4.5\times10^{13}$ |
| | C$^{34}$S 3-2 | 1.27 | 0.56 | $7.1\times10^{11}$ | $7.9\times10^{12}$ |
| | H$^{13}$CN 1-0 | 1.59 | 0.45 | $3.3\times10^{11}$ | $1.3\times10^{13}$ |
| | CN 1-0 | 8.52 | 1.92 | $1.8\times10^{13}$ | $1.1\times10^{15}$ |
| | HCN 1-0 | 14.36 | 3.48 | $8.3\times10^{12}$ | $3.1\times10^{14}$ |
| SMM2 | CS 3-2 | 8.30 | 3.10 | $5.9\times10^{12}$ | $6.5\times10^{13}$ |
| | C$^{34}$S 3-2 | 0.50 | 0.47 | $4.8\times10^{11}$ | $5.4\times10^{12}$ |
| | H$^{13}$CN 1-0 | 0.55 | 0.64 | $3.1\times10^{11}$ | $1.2\times10^{13}$ |
| | CN 1-0 | 10.22 | 3.42 | $2.6\times10^{13}$ | $1.5\times10^{15}$ |
| | HCN 1-0 | 21.67 | 4.95 | $9.1\times10^{12}$ | $3.4\times10^{14}$ |
| SMM3 | CS 3-2 | 14.76 | 2.90 | $5.7\times10^{12}$ | $6.3\times10^{13}$ |
| | C$^{34}$S 3-2 | 1.49 | 0.36 | $2.8\times10^{11}$ | $3.1\times10^{12}$ |
| | H$^{13}$CN 1-0 | 1.61 | 0.41 | $1.6\times10^{11}$ | $4.5\times10^{12}$ |
| | CN 1-0 | 9.89 | 1.90 | $2.2\times10^{13}$ | $1.3\times10^{15}$ |
| | HCN 1-0 | 17.59 | 4.69 | $1.4\times10^{13}$ | $5.2\times10^{14}$ |
| SMM4 | CS 3-2 | 14.4 | 4.30 | $1.0\times10^{13}$ | $1.1\times10^{14}$ |
| | C$^{34}$S 3-2 | 1.56 | 0.64 | $8.4\times10^{11}$ | $9.4\times10^{12}$ |
| | H$^{13}$CN 1-0 | 1.61 | 0.61 | $3.4\times10^{11}$ | $1.3\times10^{13}$ |
| | CN 1-0 | 2.72 | 0.94 | $5.7\times10^{12}$ | $3.4\times10^{14}$ |
| | HCN 1-0 | 4.04 | 1.72 | $2.6\times10^{12}$ | $9.6\times10^{13}$ |
| SMM5 | CS 3-2 | 2.56 | 1.48 | $1.8\times10^{12}$ | $2.0\times10^{13}$ |
| | C$^{34}$S 3-2 | 0.32 | 0.42 | $1.8\times10^{11}$ | $2.0\times10^{12}$ |
| | H$^{13}$CN 1-0 | 0.77 | 0.42 | $1.6\times10^{11}$ | $6.2\times10^{12}$ |
| | CN 1-0 | 10.62 | 3.17 | $2.2\times10^{13}$ | $1.3\times10^{15}$ |
| | HCN 1-0 | 13.10 | 5.15 | $8.3\times10^{12}$ | $3.1\times10^{14}$ |
| SMM6 | CS 3-2 | 8.50 | 3.2 | $5.7\times10^{12}$ | $6.5\times10^{13}$ |
| | C$^{34}$S 3-2 | 0.76 | 0.56 | $4.3\times10^{11}$ | $4.8\times10^{12}$ |
| | H$^{13}$CN 1-0 | 0.87 | 0.40 | $1.8\times10^{11}$ | $7.0\times10^{12}$ |
| | CN 1-0 | 2.97 | 0.94 | $6.2\times10^{12}$ | $3.7\times10^{14}$ |
| | HCN 1-0 | 6.84 | 1.72 | $4.3\times10^{12}$ | $1.6\times10^{14}$ |
| SMM8 | CS 3-2 | 4.51 | 2.08 | $3.1\times10^{12}$ | $3.4\times10^{13}$ |
| | C$^{34}$S 3-2 | 0.26 | 0.35 | $1.4\times10^{11}$ | $1.6\times10^{12}$ |
| | H$^{13}$CN 1-0 | 0.14 | 0.21 | $2.9\times10^{10}$ | $1.1\times10^{12}$ |
| | CN 1-0 | 4.90 | 0.84 | $1.0\times10^{13}$ | $6.2\times10^{14}$ |
| | HCN 1-0 | 20.68 | 2.40 | $1.3\times10^{13}$ | $4.9\times10^{14}$ |
| SMM9 | CS 3-2 | 12.43 | 2.70 | $8.6\times10^{12}$ | $9.5\times10^{13}$ |
| | C$^{34}$S 3-2 | 1.83 | 0.62 | $1.0\times10^{12}$ | $1.2\times10^{13}$ |
| | H$^{13}$CN 1-0 | 2.37 | 0.38 | $5.0\times10^{11}$ | $1.9\times10^{13}$ |
| | CN 1-0 | 2.96 | 0.78 | $6.2\times10^{12}$ | $3.7\times10^{14}$ |
| | HCN 1-0 | 7.26 | 1.75 | $4.6\times10^{12}$ | $1.7\times10^{14}$ |
| SMM10 | CS 3-2 | 3.58 | 1.43 | $2.5\times10^{12}$ | $2.7\times10^{13}$ |
| | C$^{34}$S 3-2 | 0.39 | 0.40 | $2.2\times10^{11}$ | $2.5\times10^{12}$ |
| | H$^{13}$CN 1-0 | 1.04 | 0.45 | $2.2\times10^{11}$ | $8.4\times10^{12}$ |
| | CN 1-0 | 10.06 | 1.85 | $2.1\times10^{13}$ | $1.3\times10^{15}$ |
| | HCN 1-0 | 14.24 | 3.50 | $9.0\times10^{12}$ | $3.4\times10^{14}$ |
| SMM12 | CS 3-2 | 9.88 | 3.26 | $6.8\times10^{12}$ | $7.5\times10^{13}$ |
| | C$^{34}$S 3-2 | 0.56 | 0.58 | $3.1\times10^{11}$ | $3.5\times10^{12}$ |
| | H$^{13}$CN 1-0 | 1.61 | 0.46 | $3.4\times10^{11}$ | $1.3\times10^{13}$ |

Table G.1: Dominant processes in CN, HCN chemistry - outflow (200K)

| Molecule | Weak UV fields $(G_0 = 10^{-3} - 10^{-1})$ | Medium UV fields $(G_0 = 10^{-1} - 10^1)$ | Strong UV fields $(G_0 = 10^1 - 10^6)$ |
|---|---|---|---|
| | | **Destruction** | |
| | $O + CN \rightarrow N + CO$ | $CN + ph \rightarrow C + N$ | $CN + ph \rightarrow C + N$ |
| | $CN + N \rightarrow C + N_2$ | $O + CN \rightarrow N + CO$ | |
| CN | | **Production** | |
| | $CNC^+ + e^- \rightarrow C + CN$ | $N + C_2 \rightarrow C + CN$ | $H + CN^+ \rightarrow CN + H^+$ |
| | $N + C_2 \rightarrow C + CN$ | $H + CN^+ \rightarrow CN + H^+$ | $HCN^+ + e^- \rightarrow H + CN$ |
| | $HCN + ph \rightarrow H + CN$ | | $N + C_2 \rightarrow C + CN$ |
| | | | $N + CH \rightarrow H + CN$ |
| | | | $HCN + ph \rightarrow H + CN$ |
| | | **Destruction** | |
| | $HCN + C^+ \rightarrow H + CNC^+$ | $HCN + C^+ \rightarrow H + CNC^+$ | $HCN + ph \rightarrow H + CN$ |
| | $HCN + ph \rightarrow H + CN$ | $HCN + ph \rightarrow H + CN$ | $HCN + C^+ \rightarrow H + CNC^+$ |
| | $HCN + HCO^+ \rightarrow CO + HCNH^+$ | | |
| HCN | | **Production** | |
| | $N + CH_2 \rightarrow H + HCN$ | $H + CCN \rightarrow C + HCN$ | $HCNH^+ + e^- \rightarrow H + HCN$ |
| | $H + CCN \rightarrow C + HCN$ | $HCNH^+ + e^- \rightarrow H + HCN$ | $H + CCN \rightarrow C + HCN$ |
| | $CN + H_2 \rightarrow H + HCN$ | | $H_2NC^+ + e^- \rightarrow H + HCN$ |
| | $C + HNC \rightarrow C + HCN$ | | $N + CH_2 \rightarrow H + HCN$ |
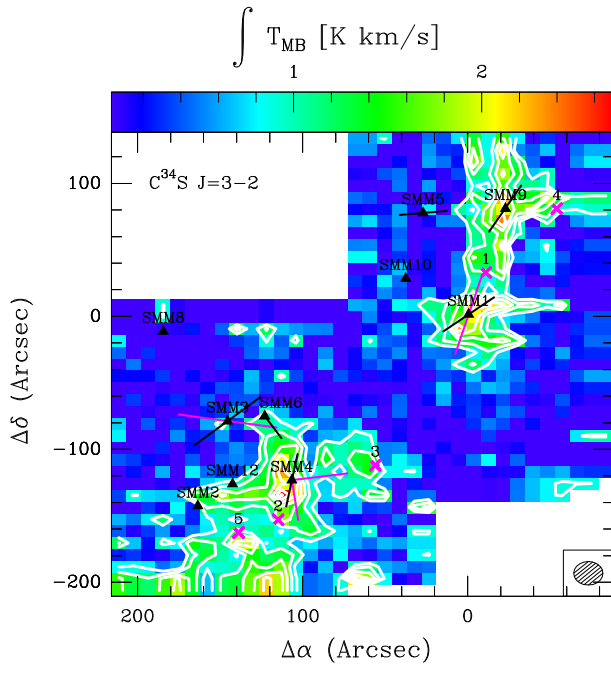
Fig. B.2: Similar to Fig. 2 but the emission of the C$^{34}$S $J = 3 - 2$
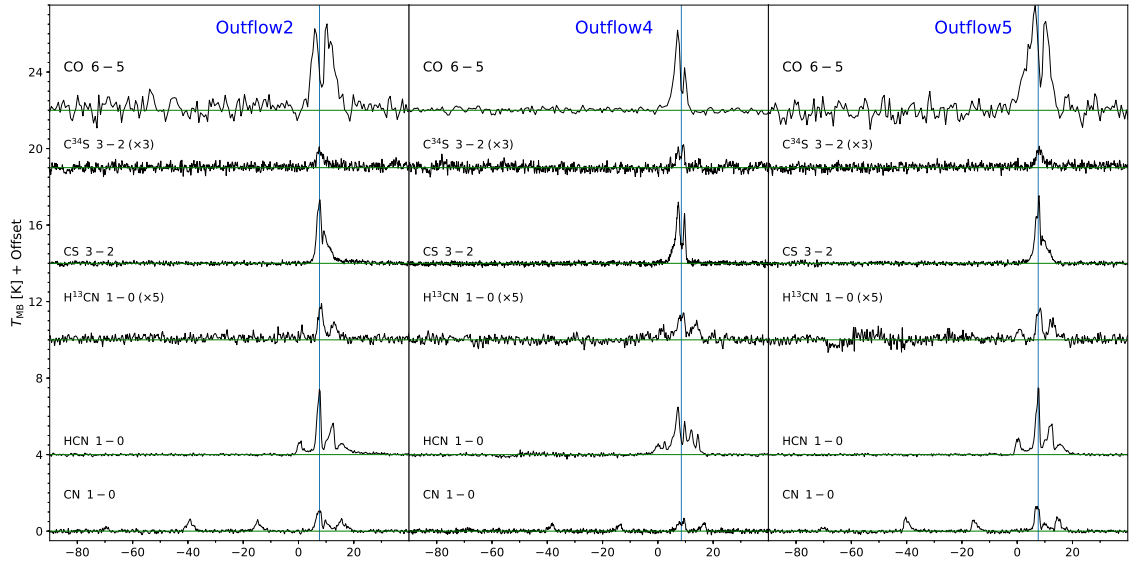line. The first contour at 30 $\sigma$ level, with step of 10 $\sigma$
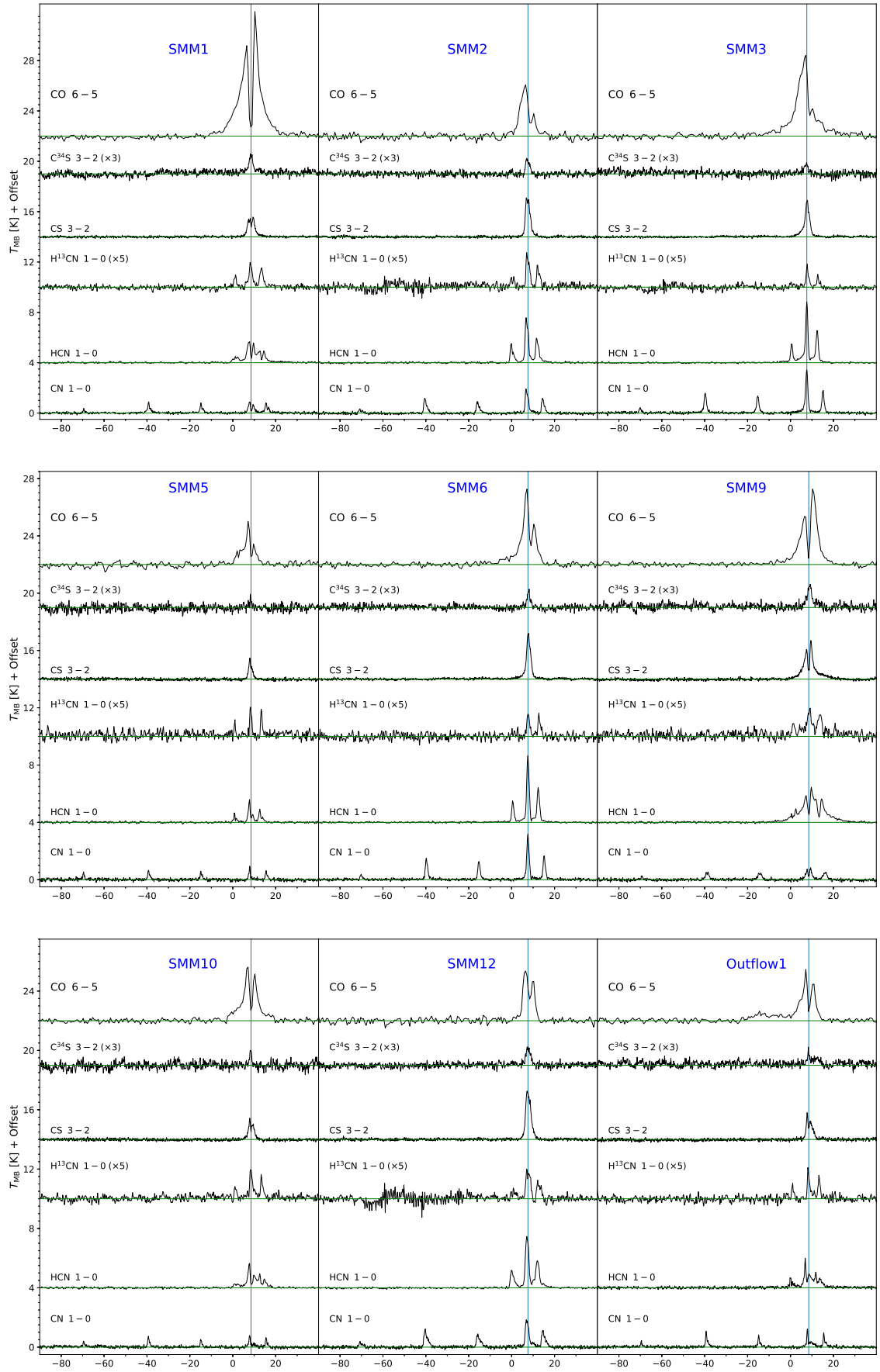
Fig. C.1: Serpens Main sources spectra of C$^{34}$S 3-2, CS 3-2 , H$^{13}$CN 1-0, HCN(1-0) abd CN(1-0) lines.
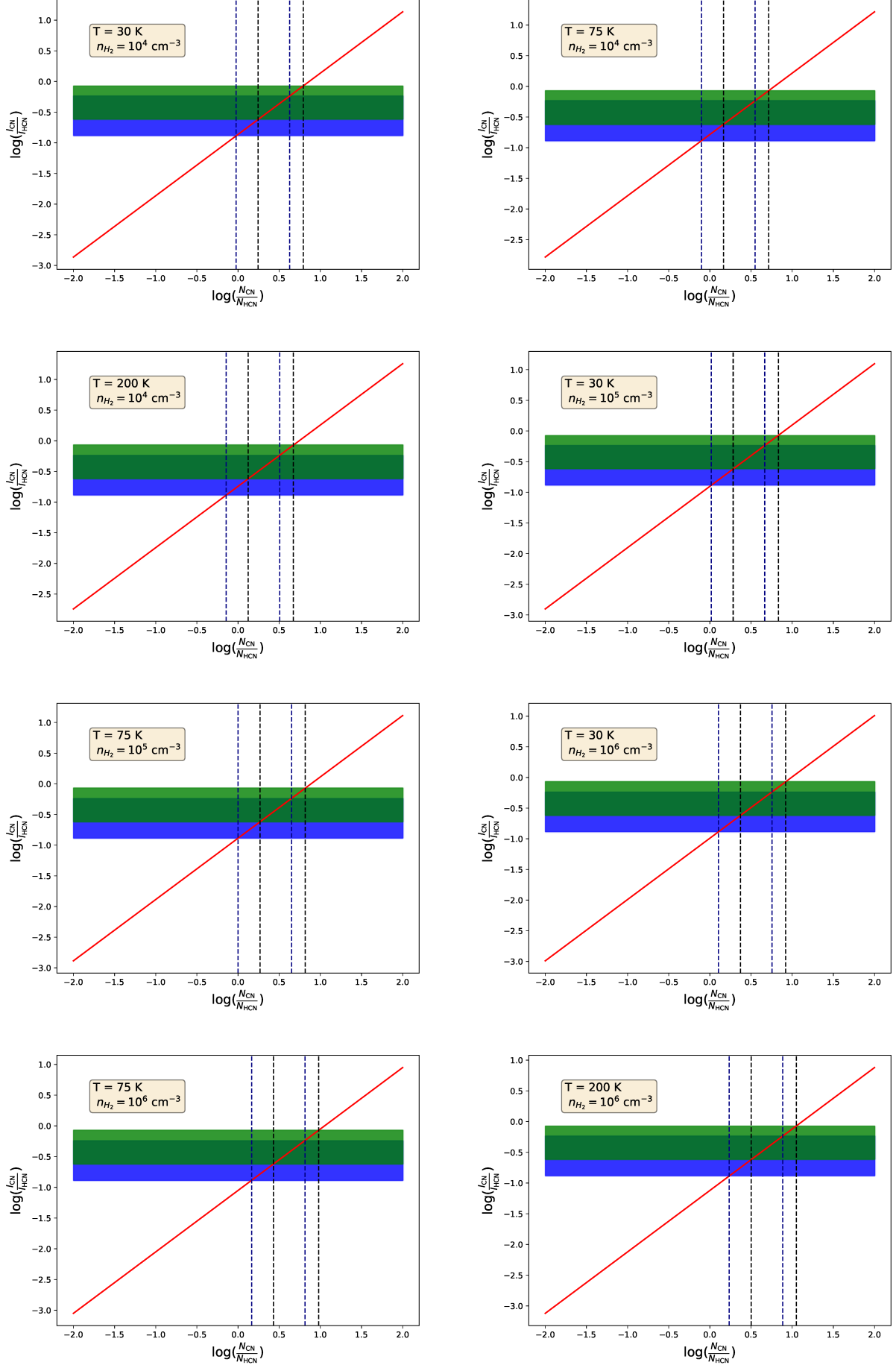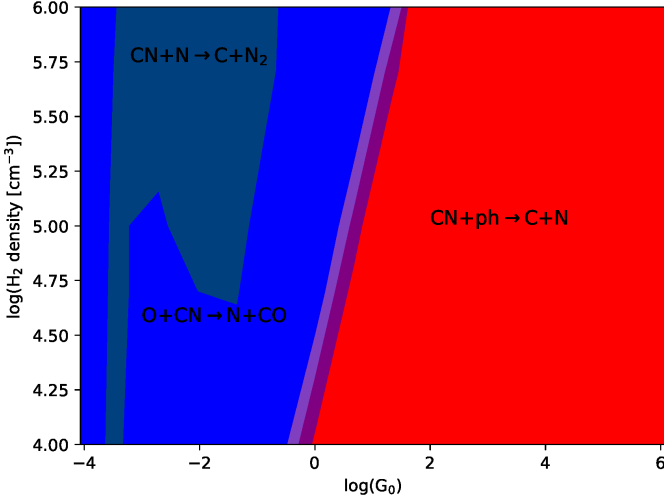
Fig. F.1: RADEX models for different parameter. Similar to Fig. 4

Fig. G.1: Dominant reactions of CN destruction. Reactions contributed at least 50% of total flux are marked with full colous. Transparent colours correspond to 30%-50% contribution.
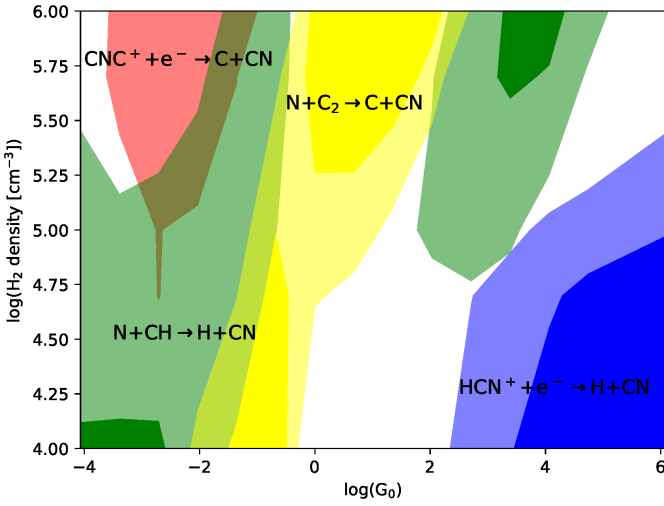


Fig. G.2: Similar to Fig. G.1 but for CN production.



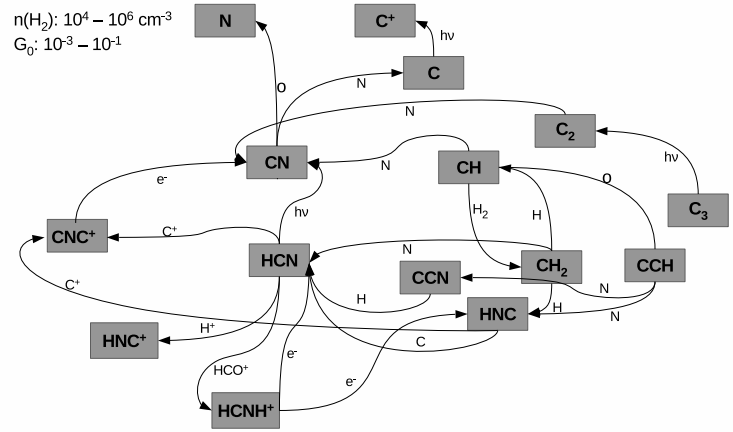Fig. G.3: Similar to Fig. G.1 but for HCN production.



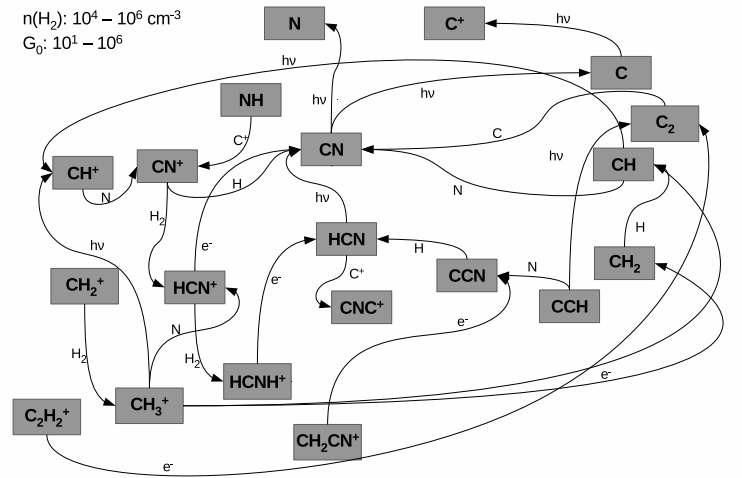Fig. G.4: Reactions network for weakly UV irradiated gas.



Fig. G.5: Similar to Fig. G.4 but for for UV field higher than $G_0 = 10^1$).